Essential Readings in Light Metals: Cast Shop for Aluminum Production.
Edited by John F. Grandfield and Dmitry G. Eskin.

Coupled modelling of air-gap formation and surface exudation during extrusion ingot DC-casting

Dag Mortensen[1], Bjørn Rune Henriksen[2], Mohammed M'Hamdi[3], Hallvard G. Fjær[1]
[1]Institute for Energy Technology, Dep. of Process and Fluid Flow Technology, Kjeller, P.O.Box 40, N-2027, Norway
[2]Elkem Aluminium, Lista, P.O.Box 128, N-4541, Norway
[3]SINTEF Materials and Chemistry, Oslo, N-0314, Norway

Keywords: Modelling, DC-casting, Finite Elements, Air-gap, Deformations, Exudation

Abstract

During casting of aluminium extrusion ingots the surface against the mould experiences a pull-in force that magnifies the air-gap during solidification close to the mould surface. This is a global phenomenon that results in early and large air-gap formations compared to the shape-casting situation. Due to the semi-solid surface created under such conditions, exudation through the surface may appear. In this study a coupled heat and fluid flow, stresses and deformation modelling tool are applied on the process. Results from the mechanical calculation are back-coupled to the thermal boundary conditions. The metallostatic head is the driving force for exudation through the dendritic network and the resulting fluid flow through this network is used to calculate a dynamic thickness of the exuded layer. Measurements from two different alloys, with rather small changes in composition, but with large variations on surface quality, are compared with the modelling results.

Introduction

It is a continuous drive in the aluminium extrusion business area to increase the productivity due to the competitiveness in the market. The introduction of air bearing mold technology like Wagstaff Airslip, Airsol Veil and Showa for the production of extrusion billets has definitively improved the billet quality by smoother surfaces with a minimum subsurface segregation zone (liquation) helping the extruders to achieve their goals. However, microstructure characterization of the subsurface reveals a higher particle density in this region relative to the bulk material which may have an influence on the extrudability, in particular for profiles with high requirements for surface finish. The presence of low melting particles is known to limit the extrusion speed because of micro tearing. But the origin of these subsurface particles, i.e. the macrosegregation and exudation phenomenon, are not fully understood. Therefore, the knowledge and understanding of these mechanisms will be essential for further improvements in the operation and the development of the mould technology.

Mathematical models which quantify surface macrosegregation due to exudation and solidification shrinkage, have been presented in the literature [1-6]. Comparisons with experimental measurements indicated that it was possible to choose input parameters leading to a good qualitative correspondence between measurements and the modelling results. In these studies, however, the length of the primary cooling zone and the position of the air gap were simply pre-set as part of the modelling input. However, since the modelled thickness and concentration of the exuded layer are very sensitive to these parameters, there is a need for a sophisticated model to predict the length of the primary cooling and air gap zones. The purpose of the present work is to propose a coupled fluid flow and thermo-mechanical model allowing for the simultaneous computation of exudation flow and air gap formation. The model is applied to the prediction of exudation for an extrusion ingot, and the modelling results are compared to experimental measurement.

Experimental

The investigated material was taken from a 254mm (10 inch) billet produced at the casthouse at Elkem Aluminium Lista using modified Showa Denko air-slip mould technology. Some details about the mould technology are found in [7]. The alloy compositions are given in Table 1.

Table 1. Chemical composition for the two alloys.

Conc. [wt%]	Si	Mg	Fe	Mn	Cu
Alloy 1 (F22)	0.43	0.37	0.21	0.04	0.005
Alloy 2 (F27)	0.63	0.46	0.23	0.17	0.15

A photograph of a typical surface of the two alloys called F22 and F27 is shown in Figure 1. The surface of F22 is clearly more smooth with less exudation.

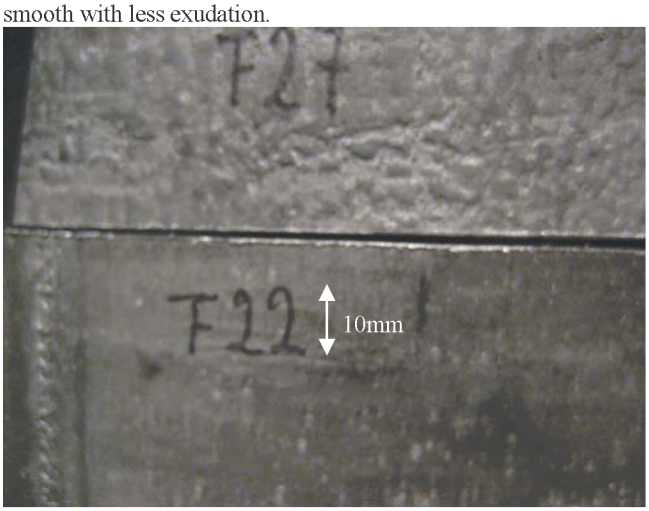

Figure 1. Photograph showing typical surface appearance for the two alloys investigated.

The samples for macrosegregation characterization of the subsurface layer were made by cutting a 3mm ring from the billet, which was subsequently cut in half and straightened. Then samples of 4x4cm size were made for OES (Optical Emission Spectrography). The samples were milled in 200µm steps to obtain a detailed macrosegregation profile in the subsurface region. The bulk macrosegregation profile was made up by OES measurements every ~10mm from the surface to the centre of the billet. The measured profiles for the outer 30mm's are shown in Figures 2 and 3. Notice the different scales on the wt%-axis.

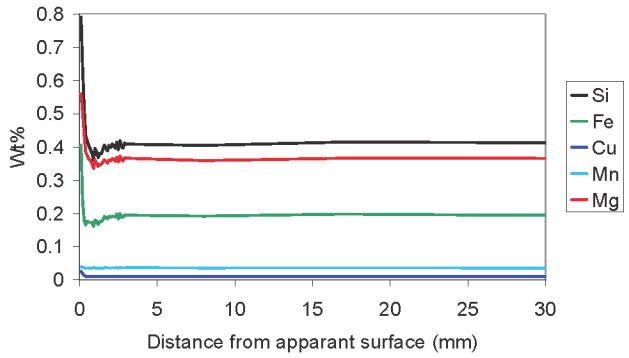

Figure 2. Measured concentration profiles for the alloy F22.

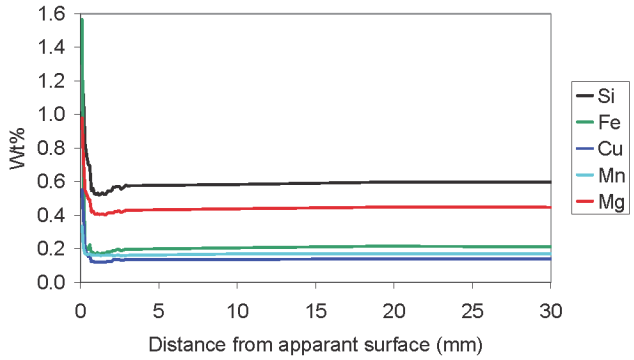

Figure 3. Measured concentration profiles for the alloy F27.

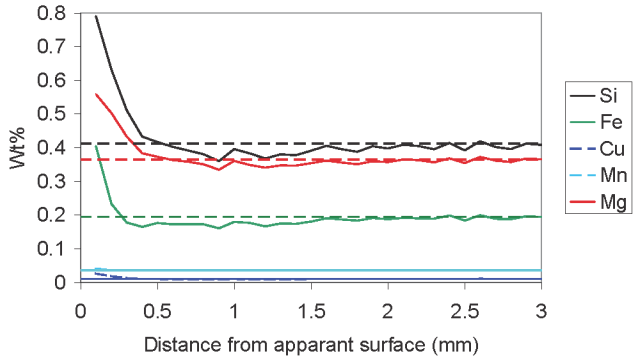

Figure 4. Close-up on the 3mm sub-surface layer of F22 including averaged concentrations.

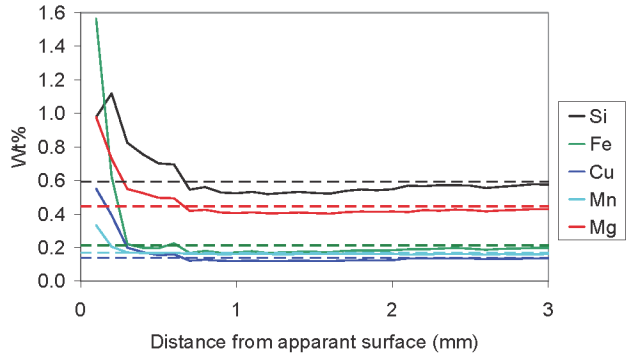

Figure 5. Close-up on the 3mm sub-surface layer of F27 including averaged concentrations.

Figures 4 and 5 show a close-up on the outer 3mm of the subsurface material with markers also for the average concentrations through the billet as estimated from the measured profiles. The measured averaged grain sizes for the two billets are shown in Figure 6.

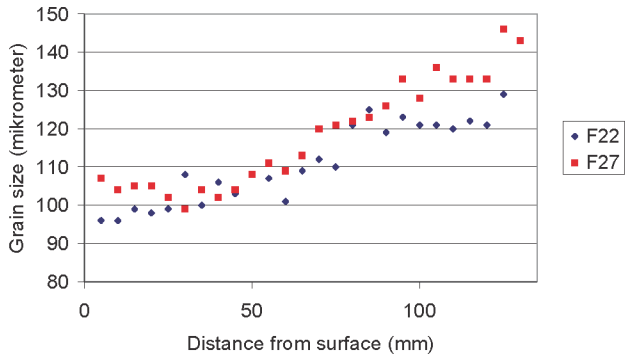

Figure 6. Measure grain size profiles for the two alloys.

In order to provide an idea about the extent of the exudated layer, surface topography measurements have been carried out using an optical technique based on a White Light Interferometer (WLI). The measurements were carried out on a band of material of ca. 3.0x40 mm^2, and 3.7x40 mm for samples F22 and F27 respectively. The measured surfaces are given in Figure 7, while the cumulative distributions of heights in the samples are given in Figure 8. In the middle of Figure 7b we can see "beads" with a typical height from bottom (blue) to top (red) of about 200µm. A typical distance from top to top is 5-10mm, compare with Fig.1.

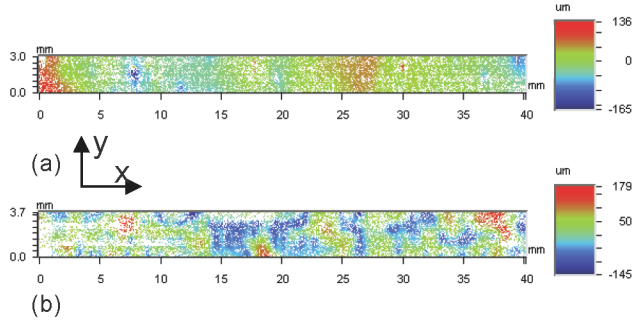

Figure 7. Measured surface topography for samples (a) F22, and (b) F27. The height positions in the samples are given relative to the average height in each sample. The casting direction corresponds to the x-direction in the figure.

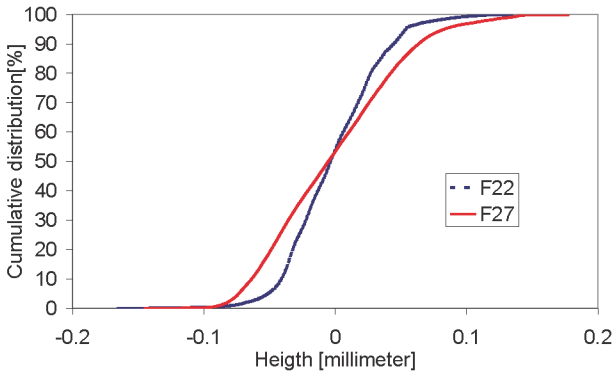

Figure 8. Cumulative distribution of the surface heights for the two alloys F22 and F27.

Modelling

The ingot thickness reduction or pull-in of the surface experienced during DC-casting is not a local phenomena, but has been found to be mainly influenced by bending/tilting and horizontal pulling on the part of the solid shell above the bottom of the liquid sump [8]. For an axial-symmetric billet the pull-in effect is reduced from hoop stresses that work against the compression of the diameter, but the larger the billet the more similar the situation is to the sheet ingot case. Bending/tilting and horizontal pulling of the solid shell are caused by deformations in the solid part *below* the bottom of the sump [8]. The result is an early formation of the air-gap as soon as the semi-solid shell against the mould is strong enough to transfer the pull-in "force" from the solid material below. When the metal leaves the mould, quite a large air-gap is already established, but at that time we are closer to the water-cooled surface below the mould. Due to upstream conductance the surface is then already closed for exudation. It is therefore during the early formation of the air-gap that most of the exudation takes place. In order to handle the modelling of air-gap formation and exudation in a semi-solid material a volume-averaged two-phase model approach is used both for the fluid flow and the stresses and deformations.

The modelling tool Alsim [9,10] was used to simulate the extrusion ingot casting process. A fully coupled heat and fluid flow, stresses and deformation calculation was performed. This simulation included the ingot, the starting block, the mould, the gas, oil and insulation (transition) rings above the mould and the hot-top. The contact area and the air-gap size against the mould was dynamically calculated by the model and back-coupled to the thermal boundary conditions. A comparison with the predicted air-gap developments against measured air-gap developments were made in [11] for a shape casting case. The modelling equations applied in this study are shortly summarized below:

Heat and fluid flow

The liquid mass and momentum equations are based on the volume-averaged two-phase model in [12]:

$$\frac{D_\omega}{\partial t}\left(\rho^l g^l + \rho^s g^s\right) - \omega_j \frac{\partial}{\partial x_j}\left(\rho^l g^l + \rho^s g^s\right) + \frac{\partial}{\partial x_j}\left(\rho^l g^l u_j^l + \rho^s g^s u_j^s\right) = 0 \quad (1)$$

$$\begin{aligned} &\frac{D_\omega g^l u_i^l}{\partial t} - \omega_j \frac{\partial g^l u_i^l}{\partial x_j} + \frac{\partial g^l u_i^l u_j^l}{\partial x_j} = -\frac{g^l}{\rho^l}\frac{\partial p^l}{\partial x_i} + \\ &\frac{\partial}{\partial x_j}\nu\left(\frac{\partial g^l u_i^l}{\partial x_j} + \frac{\partial g^l u_j^l}{\partial x_i} - u_i^s \frac{\partial g^l}{\partial x_j} - u_j^s \frac{\partial g^l}{\partial x_i}\right) + \\ &\frac{g^l}{\rho^l} f_i^l - \frac{g^l \nu}{K}\left(g^l u_i^l - g^l u_i^s\right) + u_i^s\left(\frac{\partial g^l}{\partial t} - \omega_j \frac{\partial g^l}{\partial x_j} + \frac{\partial g^l u_j^l}{\partial x_j}\right) \end{aligned} \quad (2)$$

where ρ^l, ρ^s, g^l, g^s, ω_j, u_j^l, u_j^s, p^l, ν, f_i^l and K are liquid density, solid density, liquid volume fraction, solid volume fraction, velocity of computational nodes, liquid velocity, solid velocity, liquid pressure, kinematic viscosity, external forces and permeability, respectively. $D_\omega/\partial t$ denotes the time derivative of a variable moving with the velocity of the computational grid. Solidification shrinkage, interfacial friction, momentum transfer due to phase change and macroscopic viscous stress contribution are included, for more details see [12]. The permeability of the semi-solid material is assumed to follow the Kozeny-Carman relation:

$$K = \frac{l_m^2}{180}\frac{g_l^3}{\left(1-g_l\right)^2} \quad (3)$$

where l_m is a characteristic length of the microstructure. In our case, with a grain-refined close to globulitic microstructure the measured average grain size 5mm from the surface was selected, 96μm for alloy F22 and 107μm for alloy F27.

In this study the solid velocity in equations (1) and (2) has been assumed equal to the casting velocity of the billet which was 82mm/min for alloy F22 and 78mm/min for alloy F27. For the lower part of the mushy zone where exudation appears and the liquid pressure drops to very low values this approximation is valid. These mass and momentum equations have been implemented into Alsim. The numerical solution applies in principle the same techniques as in [9]. For energy conservation the mixture equation in [9] was applied.

Stresses and deformations

The mechanical analysis is carried out in the fully solid regions of the ingot as well as in the coherent part of the mushy zone. The upper boundary of the coherent mushy zone corresponds to a solid volume fraction equal to 0.6 in this study. For a complete description of the mechanical model employed, see [13]. Here only a brief description is provided. Denoting the solid stress σ_s, the mixture momentum balance in the coherent part of the mushy zone can be expressed by:

$$\nabla\cdot\left[g_s\boldsymbol{\sigma}_s\right] - \nabla\left[g_l\mathbf{p}_l\right] + \left[\boldsymbol{\rho}_s\mathbf{g}_s + \boldsymbol{\rho}_l g_l\right]\mathbf{g} = \mathbf{0} \quad (4)$$

where **g** is the gravity vector. The model formulation has been based on the classical small deformation theory where the total strain e, derivable from the displacement field u is subdivided into viscoplastic, elastic and thermal components.

$$\boldsymbol{\varepsilon} = \frac{1}{2}\left(\nabla\mathbf{u} + \left[\nabla\mathbf{u}\right]^t\right) = \boldsymbol{\varepsilon}^{vp} + \boldsymbol{\varepsilon}^e + \boldsymbol{\varepsilon}^T \quad (5)$$

The thermal strain component can be written as an integral of the (volumetric) thermal expansion coefficient β_T.

$$\boldsymbol{\varepsilon}^T = -\frac{1}{3}\int_T^{T_{coh}} \beta_T(T)dT\cdot\mathbf{I} \quad (6)$$

The constitutive equation for elasticity (Hook's law) defines how the stress depends on the elastic strain $\boldsymbol{\varepsilon}^e$ and the temperature dependent Young's modulus and Poisson's ratio entering the matrix **D**.

$$\boldsymbol{\sigma} = \mathbf{D}(T)\cdot\boldsymbol{\varepsilon}^e \quad (7)$$

Constitutive equations for the viscoplastic deformation of aluminium alloys during solidification are based on the work of Ludwig [14], where the mushy zone is considered as a partially cohesive porous solid saturated with liquid:

$$\dot{\varepsilon}_s^p = \frac{\dot{\varepsilon}_0 e^{-\frac{Q}{RT}}}{\left(C\sigma_0\right)^n}\left[-\frac{1}{9}A_2(g_s)J_1\mathbf{I} + \frac{3}{2}A_3(g_s)g_s\boldsymbol{\tau}_s\right]\left[\frac{1}{9}A_2(g_s)J_1^2 + 3A_3(g_s)J_2\right]^{\frac{n-1}{2}} \quad (8)$$

$$\dot{C} = \alpha\left(g_s, X\right)\left(1 - \frac{C}{C^*\left(g_s, X\right)}\right)\bar{\dot{\varepsilon}}_s^p \quad (9)$$

J_1 and J_2 are the first and second invariants of the effective stress tensor $\hat{\boldsymbol{\sigma}}_s = \left(g_s\boldsymbol{\sigma}_s - g_l p_l \mathbf{I}\right) + p_l \mathbf{I}$, $\boldsymbol{\tau}_s$ is the solid deviatoric stress tensor, $\bar{\dot{\varepsilon}}_s^p$ is the effective strain rate, and X is the stress triaxiality. Equation (9) describes the evolution of the partial cohesion of the coherent mushy zone. Expressions for the solid fraction and triaxiality dependent functions, A_2, A_3, and C* are all given in [13]. In the fully solid regions (g_s=1, A_2=0, A_3=1, C=1), equation (4) simplifies to the usual Cauchy's equation for a fully solid material

$$\nabla \cdot \boldsymbol{\sigma}_s + \boldsymbol{\rho}_s \mathbf{g} = \mathbf{0} \tag{10}$$

A set of equations assuming steady state creep above a temperature T_0 and work hardening below this temperature, are applied for viscoplastic deformation in the fully solidified regime:

$$\bar{\sigma} = F(T) \cdot \left(\phi_0 + \phi\right)^{n(T)} \cdot \left(\dot{\bar{\varepsilon}}_p\right)^{m(T)} \tag{11}$$

$$d\phi = \begin{cases} d\bar{\varepsilon}_p & \text{when} \quad T \le T_0 \\ 0 & \text{when} \quad T > T_0 \end{cases} \tag{12}$$

Thermo-fluid-mechanical coupling

The resulting stresses and displacements affect the thermal boundary conditions regarding contact zones or air gaps between ingot and mold. On the boundaries between two different materials the heat transfer coefficient α is calculated according to:

$$\alpha = Min\left(\alpha_{Contact}, \alpha_{gap}\right) \tag{13}$$

where the gap heat transfer coefficient α_{gap} is calculated by:

$$\alpha_{gap} = \frac{1}{\frac{1}{\alpha_{conduction} + \alpha_{radiation}} + \frac{1}{\alpha_{contact}}} \tag{14}$$

where the local displacement dependent gap value and the local exudation thickness is used to calculate the conduction heat transfer through the gap $\alpha_{conduction}$, and the radiation part $\alpha_{radiation}$ is found from the local temperatures and emissivities on the two boundaries. Based on measurement of mould temperatures in [7] $\alpha_{contact}$ has been found to be about 900W/m^{2}K for the stationary phase with established air-slip.

Fluid outflow from the semi-solid surface is only allowed if there is a local air-gap at the current element surface. The local air-gap value is a result of the local displacements and the local exudation thickness (a large outflow will close the air-gap). With no air-gap the fluid outflow is hindered by the solid mould surface. Due to numerical considerations of what to be handled as a real air-gap the minimum air-gap size for exudation was set to 1 micrometer in this study. If the calculated air-gap is larger than 1μm a pressure boundary condition is applied in the solution of the liquid mass and momentum equations. The pressure at the melt surface is equal to zero and the pressure at the local air-gap surface is calculated from the height of the metal column above the surface. This pressure drop is then the driving force for the fluid outflow, while the pressure drop through the semi-solid material is the limiting factor. More details about thermal and mechanical boundary conditions can be found in [7].

Material properties

Thermal properties for the two alloys were calculated by the microstructure model Alstruc [15]. The resulting liquid fraction as function of temperature is shown in Figure 9.

For the mechanical properties the F(T), n(T) and m(T) functions in equation (11) were taken from the 6063-alloy in [16] for the alloy F27, while data for a 6060-alloy measured in a similar manner as reported in [16] were used for F22. The parameters for the cohesion mechanical model of the semi-solid material were taken from [14], as measured for a grain-refined AlCu-alloy.

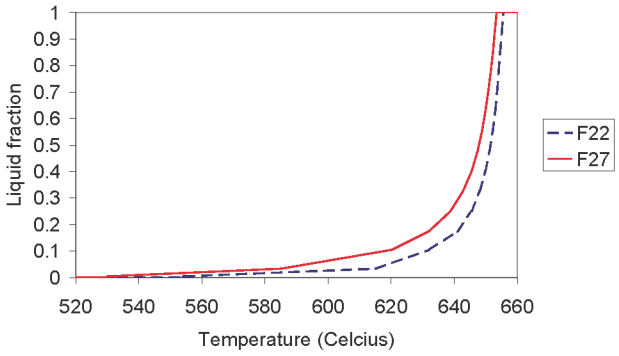

Figure 9. Solidification paths for the two alloys. Solidus and liquidus temperatures are 553.9/529.6 and 655.6/653.5 for F22/F27, respectively.

Results

The start finite element geometry of the simulations is shown in Figure 10. During casting elements are expanded in one row of elements marked with expansion zone below.

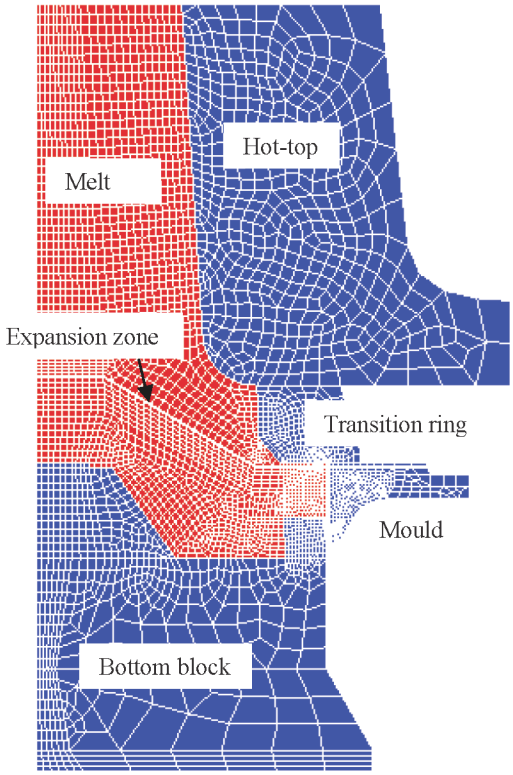

Figure 10. Finite element start mesh.

The fluid flow at 200 seconds from start of simulation is shown in Figure 11. Please note that it is the product of the liquid volume fraction g^l and the liquid velocity u_i^l that is shown as velocities.

Maximum velocities in pure liquid are up to 23mm/seconds at this time of the simulation. Highest velocities are in the region below the transition ring and further down along the sump. The velocities shown here are a continuous field from pure liquid down to the solidus including the shrinkage effect. A focused view of the velocities in the mould region is shown in Figure 12. Clamping (cutting) of velocity arrows has been applied in Figure 12 in order to show also smaller velocities.

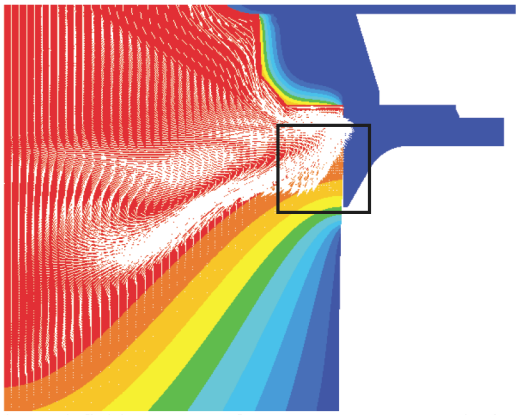

Figure 11. Thermal field, contours from 100 to 700°C, velocity field ($g^l u_i^l$) and displacement field for the alloy F27 at 200 seconds from start of simulation.

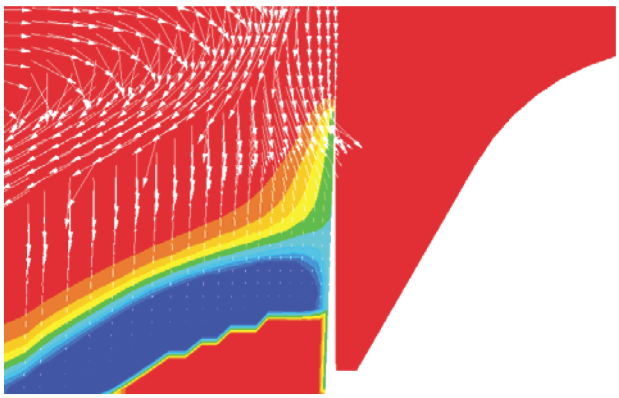

Figure 12. Pressure field, contours from –10000 to 0 Pascal, velocity field (clamping on) and displacement field for the alloy F27 at 200 seconds from start of simulation.

The calculated accumulated exudation thickness along the mould surface is shown for the two alloys in Figure 13 and 14. Together with the exudation thickness is shown the calculated air-gap size, the inward displacement of the surface (R-disp), the horizontal velocity component of $g^l u_i^l$ at the surface (X-vel) (all left axis values) and solid volume fraction (right axis value).

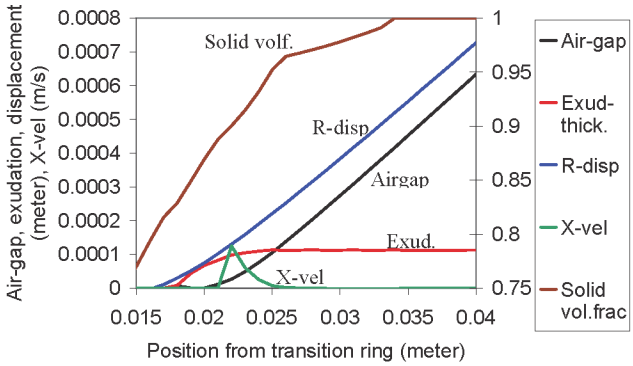

Figure 13. Air-gap, exudation thickness, inward surface displacement, horizontal surface velocity component (left hand axis values) and solid volume fraction (right hand axis values) for the alloy F22.

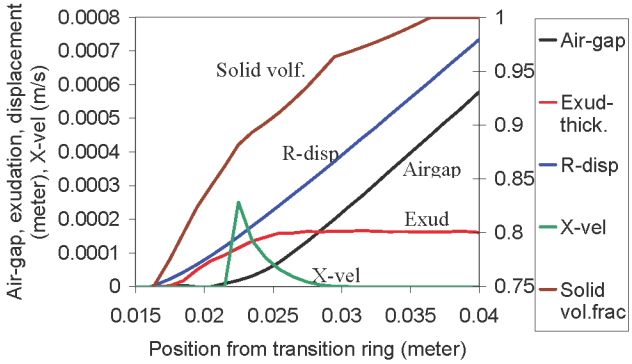

Figure 14. Air-gap, exudation thickness, inward surface displacement, horizontal surface velocity component and solid volume fraction for the alloy F27.

Discussion

We believe that the highest concentrations close to the surface of the billet are inside the layer of exuded material. For the alloy F27 we can see from Figure 5 that the concentrations are rising sharply at positions 0.2 and 0.1mm from the surface with e.g. iron concentrations 3 and 7 times higher than the average concentration. At 0.3mm from the surface the iron concentration is similar to the average concentration. Silicon and manganese concentrations rise above average level already at 0.6mm from the surface but this is probably due to shrinkage effects. At 0.1-0.2mm from the surface we are at concentrations levels twice above averaged concentrations. Similar for alloy F22 we can observe from Figure 4 that we are on concentration levels twice the average concentrations for the outermost measurement point, at 0.1mm from the surface. Please note that these measurements does not fully represent the variations we have close to the surface, they are merely to be interpreted as arbitrary samples from the surface.

However, the above observations based on measured surface macrosegregation are supported by measurements of the surface roughness, although we do not know from these measurements the position of the original surface. Further metallographic analyses would be needed to be more specific about the original surface. However, from Figure 8, we can read that about 95% of the

surface for alloy F27 are in the interval –0.1mm to +0.1mm from an average level and similar for F22 the main part of the surface are in the interval –0.7mm to +0.7mm. So calculated exudation thicknesses in the range of 0.1-0.2 mm for F22 and F27 are supported by the surface roughness measurements.

For the depleted sub-surface layer this has significantly lower concentrations than the average concentrations in a range from about 0.5mm to 2.5mm from the surface, so a typical thickness of about 2mm, although it can be argued that the depleted layer goes deeper since the concentrations very slowly rise against averaged values from 2-3mm to 20mm depths inside the surface, see Figures 2 and 3.

Our model results for the two alloys fit very well with observations above, especially taken into account that no fitting was done for the calculations. We have only used solidification paths as calculated by Alstruc, grain sizes as measured and casting parameters from production together with a volume averaged fluid mass and momentum model including shrinkage coupled with deformation in order to produce very reasonable results for this process. The calculated averaged exudation thickness for F22 and F27 are 0.11 and 0.16mm, respectively, see Figures 13 and 14. This result give us confidence in that future modelling work regarding the influence of process parameters on the resulting exudation levels make sense to do. Precipitation of particles in the enriched sub-surface layers is believed to be of importance for further downstream processing, and it is of interest to understand as much as possible the mechanism behind the formation of the particles during casting.

The calculation of the air-gap is of course crucial for the predictive capabilities of the model including how to treat the semi-solid material mechanically, in this case with the cohesion model. It also showed up during our work that the back-coupling from exudation thickness to the effective air-gap size was a necessary part of the model. The exudation increases the effective contact length against the mould, and thereby increases the solid fraction at the surface in the air-gap where exudation is possible. The initial exudation is filling the narrow gap completely as can be seen from figures 13 and 14. The thickness of the exuded layer follows the size of the inwards displacement of the surface (the red and the blue curve) which results in a zero air-gap value – so the surface is closed for further exudation in this range. Note also the similar development of the two curves for each alloy in this range, where the exudation thicknesses grow as fast as the inward displacements of the surfaces. Since the exuded liquid in this area closes the gap, "beads" on the surface are not expected to be formed from this mechanism. It is first when the air-gap grows faster than the exuded layer that we can expect "beads" on the surface. At this point (about 22mm from the transition ring) the surface solid fraction is lower for F27 than for F22, so the exuded layer continues to grow significantly for F27, but not for F22 which is almost finished at this point. This explains the greater tendency for beads on F27 as can be seen in Figure 1. But both alloys experiences exudation limited by the air-gap, as evident from the macrosegregation profiles close to the surface. The difference in exudation thicknesses between the two alloys are mainly due to the different thicknesses of the mushy zone. F27 with a higher alloy content and thicker mushy zone will then obtain the necessary strength of the coherent semi-solid material at a lower surface solid fraction, thereby creating more exudation.

A numerical test applying the same mechanical constitutive parameters for F27 as for F22 did not show a significant change. Also using the grain size measured for F22 in the calculation of the permeability for F27 did not show a significant change.

Conclusions

The modelled exudation phenomena in this study have been found to consist of two different phases. In the first phase the growth of the exuded layer is constricted by the development of the surface displacement (pull-in), and the room between the original surface and the mould surface is completely filled with exuded liquid. In the next phase the air-gap grows faster than liquid flowing out of the original surface, and in this phase beads on the surface may form. Our hypothesis is that the observed difference in surface appearance for the two different alloys stem from the second phase, while the first phase of the exudation are similar for the two alloys. In the second phase the alloy with the thicker mushy zone has a lower surface solid fraction at the point where the air-gap grows faster than the exuded layer, and therefore significantly more exudation are formed as beads for this alloy.

Acknowledgements

Funding of this work by Elkem Aluminium ANS and the EUREKA project E!3725 Casting Top Models (CTM) is gratefully acknowledged. The mathematical model Alsim used in this study is currently under development in the CTM-project with participation from Aleris International Inc., Corus Technology BV, Elkem Aluminium ANS, Hydro Aluminium AS, Institute for Energy Technology, Netherlands Institute for Metal Research and SINTEF Materials and Chemistry, and with support from the Research Councils of Netherlands and Norway.

References

[1] E. E. Emley. Continuous casting of aluminium. *International Metals Reviews*, pages 75–115, June 1976. Review 206.

[2] A. Mo. Mathematical modelling of surface segregation in aluminium DC casting caused by exudation. *International Journal of Heat and Mass Transfer*, **36**(18):4335–4340, 1993.

[3] E. Haug, A. Mo, and H. J. Thevik. Macrosegregation near a cast surface caused by exudation and solidification shrinkage. *International Journal of Heat and Mass Transfer*, **38**(9):1553–1563, 1995.

[4] A. Mo, T. Rusten, H. J. Thevik, B. R. Henriksen, and E. K. Jensen. Modelling of surface segregation development during DC casting of rolling slab ingots. In R. Huglen, editor, *Light Metals*, pages 667–674, Warrendale, PA, USA, 1997. TMS-AIME.

[5] H. J. Thevik, A. Mo, and T. Rusten. A mathematical model for surface segregation in aluminium DC casting. *Metallurgical and Materials Transactions B*, **30B**:135–142, 1999.

[6] M. Mhamdi, A. Mo, D. Lindholm, and D. Mortensen. Mathematical modelling of surface segregation in DC casting of multicomponent aluminium alloys. In P. R. Sahm, P. N. Hansen, and J. G. Conley, editors, *Modelling of casting, welding and advanced solidification processes – IX*, pages 656–663. Shaker Verlag, 2000.

[7] D. Mortensen, B.R. Henriksen, J. Hvistendahl, H.G. Fjær, "Modelling of mould toe-in during extrusion ingot DC-casting", *Light Metals 2007*, TMS, Warrendale, PA, pp715-720.

[8] H. G. Fjær and A. Håkonsen, "The mechanism of pull-in during DC-casting of aluminium sheet ingots", *Light Metals 1997*, TMS, Warrendale, PA, pp683-690.

[9] D. Mortensen, "A mathematical model of the heat and fluid flows in direct-chill casting of aluminium sheet ingots and billet",

Metallurgical and Materials Transactions, 30B, (1999) pp119-133.
[10] H.G. Fjær and A. Mo, "ALSPEN – A mathematical model for thermal stresses in DC casting of aluminium billets", *Metallurgical Transactions*, 21B, (1990) pp1049-1061.
[11] J. Grandfield et.al., "Remelt ingot mold heat flow and deformation", *Light Metals 2006*, TMS, Warrendale, PA, pp869-876.
[12] J. Ni and C. Beckermann, "A volume-averaged two-phase model for transport phenomena during solidification", *Metall. Trans. B*, 1991, vol.22B, pp.349-361.
[13] M. M'Hamdi, A. Mo and H.G. Fjær, "TearSim: A two-phase model addressing hot tearing formation during aluminium direct chill casting", *Metall. Trans. A*, 2006, vol.37A, pp.3069-3083.
[14] O. Ludwig, Ph.D. Thesis, Institut National Polytechnique de Grenoble, Grenoble, Feb. 2004.
[15] A.L. Dons et.al., *Metall. Trans. A*, 1999, vol.30A, pp.2135-2146.
[16] W.M. van Haaften, "Constitutive behaviour and hot tearing during aluminium DC casting", PhD-Thesis TUDelft, The Netherlands, 2002. ISBN 90-9015792-1